THE UNIVERSITY *of* EDINBURGH
School of Physics
and Astronomy

Senior Honours Project

Understanding Bond-Dependent Exchange in $CoTiO_3$: A Green's Function Approach

Nishwal Gora
March 2025

Abstract

This report uses a Green's function response model to describe the spin-wave excitations in $CoTiO_3$. A key focus of this paper is the development of the mathematical framework required for this approach, which has not previously been applied to this compound. Central to our treatment is the incorporation of a rotating frame formalism alongside a precise description of the single-ion physics of Co^{2+}. Our initial findings highlight the need to include the strong bond-dependent exchange interactions identified in earlier studies [1–3]. To account for these interactions, we employ Resonating Valence Bond (RVB) theory [4], proposing that the anisotropy arises from the formation of dimers between antiferromagnetic spins oriented out of the plane. We validate the physical consistency of our model by deriving a Curie–Weiss temperature of $\theta_{\mathrm{CW}} = 17.4\,\mathrm{K}$ and constraining both the nearest-neighbour exchange and molecular field terms to approximately 4.0 ± 0.2 meV. Ultimately, this work aims to reintroduce dimer formation as a plausible mechanism underpinning bond-dependent exchange anisotropy in complex oxides like $CoTiO_3$, thereby opening the door to further studies on cobaltates as candidates for spin-liquids.

Declaration

I declare that this project and report is my own work.

Signature: Nishwal Gora Date: 28/03/2025

Supervisor: Prof. Chris Stock 10 Weeks

Contents

1 Introduction **2**

2 Background: Linear Response Theory **3**
2.1 Scattering Cross-Section 3
2.2 Using Green's Functions 4
2.3 Magnetic Hamiltonian 5
2.3.1 Single-ion excitations ($\mathcal{H}_1$) 6
2.3.2 Inter-ion excitations ($\mathcal{H}_2$) 6

3 Method: Linear Response Theory in the specific case of $CoTiO_3$ **7**
3.1 Structure and Crystal Electric Field 7
3.2 Additional perturbations on $^4T_1$ 9
3.3 $\mathcal{J}(\mathbf{Q})$ and the need for a Rotating Frame 10
3.3.1 Step 1: Intra-Cell Rotation within the "Spin Unit Cell" 11
3.3.2 Step 2: Rotation of the Entire Unit Cell 12
3.3.3 Green's Function in the Rotating Frame and Final Transformation . 12

4 Results and Discussion: Dimers and Bond-Dependent exchange **13**
4.1 Initial Findings 13
4.2 The need for bond-dependent exchange 14
4.2.1 Resonating Valence Bond Theory 15
4.2.2 Energy Comparison Between the Néel State and Singlet State . . . 15
4.2.3 Lattice Distortions and the Breaking of Exchange Equivalence . . . 16
4.2.4 Modelling Anisotropic Exchange 17
4.3 The Anisotropic Exchange Model and its physical implications 17

5 Conclusion and Future Research **20**

1 Introduction

Recent neutron scattering experiments on $CoTiO_3$ have revealed several intriguing magnetic phenomena. For instance, elastic neutron scattering studies demonstrated that as the external magnetic field increased from 0 T to 7.5 T, the magnetic order of $CoTiO_3$ evolved from a conventional antiferromagnetic state to a monodomain canted structure [5]. Moreover, inelastic neutron scattering measurements uncovered a distinct spin-wave excitation gap of approximately $\Delta = 1.0\,\text{meV}$ at zero external field, a feature that was successfully modelled using an XXZΔ framework [6]. These observations, specifically the latter, highlight the rich and complex magnetic behaviour of $CoTiO_3$, making its magnetic properties a compelling subject for further theoretical investigation.

This report is situated within a broader effort to understand the effects of spin–orbit coupling in magnetic materials. Interactions such as the Dzyaloshinskii–Moriya and Kitaev couplings, which arise from strong spin–orbit effects, have thus far been pivotal in explaining exotic magnetic ordering in multiferroic systems [7, 8]. In particular, octahedrally coordinated Co^{2+} compounds such as $CoTiO_3$ have attracted significant attention because bond-dependent exchange interactions appear to play a crucial role in determining their magnetic properties [1–3].

Liu and Khaliullin [2] extended the Kitaev model—originally formulated for d^5 Mott insulators—to d^7 systems such as Co^{2+} in octahedral environments. They argued that the presence of a spin–active e_g electron in cobaltates introduces distinct interaction patterns, giving rise to both Heisenberg and Kitaev-type couplings. This bond-dependent exchange mechanism has the potential to stabilise spin–liquid phases by favouring Kitaev interactions over traditional Heisenberg couplings, thereby addressing some of the unresolved questions in magnetic frustration and quantum magnetism.

However, recent experimental investigations by Hoffmann et al. [9] revealed that structural distortions occur in $CoTiO_3$ below its Néel temperature, indicating significant magnetostructural coupling. The observed lattice anomalies along specific crystallographic axes imply a reduction in symmetry that is essential to accommodate bond-dependent exchange interactions. Such evidence may provide strong experimental support for non-Kitaev theories, including those involving dimerisation, which require structural distortions to form exotic magnetic states.

In this paper, we aim to propose a novel theory for bond-dependent exchange in $CoTiO_3$, by appealing to Resonating Valence Bond Theory (RVB) and dimer formation. The layout of the paper is as follows. In Section 2, we build a general linear response theory approach, linking the neutron magnetic cross section to Green's functions, which model the excitations of spin-waves. Crucial to this approach are both the single-ion and inter-ion Hamiltonians, which respectively describe the excitations within the local Co^{2+} environment and the propagation of these excitations throughout the lattice. The Hamiltonian is incorporated into the Green's function to explain the evolution of the response. In this section, the model is constructed in full generality, establishing the framework upon which our subsequent analysis is based.

In Section 3, we construct the Hamiltonian specific to $CoTiO_3$, incorporating a ro-

tating frame formalism to account for the compound's noncollinear magnetic structure. Once this specific model is in place, Section 4 presents the plotted dispersion relations. Here, we identify key discrepancies and address them by proposing dimer formation along the J_4 direction. This research is crucial because cobaltates are increasingly regarded as promising spin-liquid candidates [1, 2], and understanding the delocalisation and breakdown of long-range order which may arise with dimer formation [4] can greatly contribute to the field. .

2 Background: Linear Response Theory

2.1 Scattering Cross-Section

Spin-waves represent the collective fluctuations of individual magnetic moments due to thermal agitation and quantum zero-point motions [10]. These excitations (known as magnons), which are analogous to phonons, possess an energy $\hbar\omega$ and propagate with a wavevector $\hbar\mathbf{q}$. When the magnetic dipole of a neutron interacts with a magnon, it scatters, resulting in a change in both the wavevector and energy; in this report, these changes are denoted by $\mathbf{Q}$ and ω, respectively.

To model these spin waves, we plot their dispersions, which are given by the neutron magnetic cross section. The neutron magnetic cross section is directly proportional to the spin structure factor. In particular, it can be expressed as [11]

$$S(\mathbf{Q},\omega) = g_L^2 f^2(\mathbf{Q}) \sum_{\alpha\beta} \left(\delta_{\alpha\beta} - Q^\alpha Q^\beta\right) S^{\alpha\beta}(\mathbf{Q},\omega), \tag{1}$$

where $f(\mathbf{Q})$ is the magnetic form factor [12, 13], g_L is the Lande g factor and $S^{\alpha\beta}(\mathbf{Q},\omega)$ is the spin structure factor. For a Co^{2+} crystal, the magnetic form factor, which is the Fourier transform of the magnetisation of a single magnetic atom, can be written in its analytic form,

$$f(\mathbf{Q}) = Ae^{-a|\mathbf{Q}|^2} + Be^{-b|\mathbf{Q}|^2} + Ce^{-c|\mathbf{Q}|^2} + D,$$

with the coefficients A, B, C, D, a, b, and c provided in the International Tables for Crystallography [14].

Physically, $S^{\alpha\beta}(\mathbf{Q},\omega)$ quantifies the response of the crystal to an external perturbation (here, the scattering neutron) as a function of momentum transfer $\mathbf{Q}$ and energy transfer ω. Mathematically, $S^{\alpha\beta}(\mathbf{Q},\omega)$ is obtained as the Fourier transform of the time-dependent correlations between spin operators in the crystal. Importantly, in Co^{2+}, the orbital angular momentum is effectively quenched, $\langle\hat{\mathbf{L}}\rangle = 0$, so that the contributions from orbital angular momentum are minimal [15], and we will focus on spins.

The spin-spin correlation function is defined as

$$\langle S^\alpha(\mathbf{Q},t) S^\beta(-\mathbf{Q},0)\rangle,$$

where $S^\alpha(\mathbf{Q},t)$ is the spin operator for the α component of the spin at time t for momentum transfer $\mathbf{Q}$, and $S^\beta(-\mathbf{Q},0)$ is the corresponding operator at time zero with the

opposite momentum. Fourier transforming this correlation function in time gives the spin structure factor:

$$S^{\alpha\beta}(\mathbf{Q},\omega) = \frac{1}{2\pi}\int_{-\infty}^{\infty} dt\, e^{i\omega t}\langle S^{\alpha}(\mathbf{Q},t)S^{\beta}(-\mathbf{Q},0)\rangle.$$

This expression introduces the energy transfer, ω—which reflects the frequency of the spin fluctuations—and simultaneously characterises how the crystal responds to external perturbations at specific momentum, $\mathbf{Q}$, and energy, ω, values. This connection is established through the fluctuation-dissipation theorem, which links the observed spin fluctuations to the system's response function as represented by the Green's function, $G^{\alpha\beta}(\mathbf{Q},\omega)$.

2.2 Using Green's Functions

To establish a connection between the spin structure factor and the system's response, we begin with the definition of the retarded Green's function:

$$G^{\alpha\beta}(\mathbf{Q},t) \equiv G^{\alpha\beta}(\hat{S}^{\alpha}(\mathbf{Q},t),\, \hat{S}^{\beta}(-\mathbf{Q},0),t) \;=\; -\,i\,\Theta(t)\,\big\langle\big[\hat{S}^{\alpha}(\mathbf{Q},t),\, \hat{S}^{\beta}(-\mathbf{Q},0)\big]\big\rangle, \qquad (2)$$

where $\Theta(t)$ is the Heaviside step function ensuring causality, and $\langle[\hat{S}^{\alpha}(\mathbf{Q},t),\hat{S}^{\beta}(-\mathbf{Q},0)]\rangle$ describes the time evolution of the spin operators. The first step in the derivation is to take the time derivative of $G^{\alpha\beta}(\mathbf{Q},t)$ and use the Heisenberg equation of motion,

$$i\,\frac{d}{dt}\,\hat{S}^{\alpha}(\mathbf{Q},t) \;=\; \big[\hat{S}^{\alpha}(\mathbf{Q},t),\, \mathcal{H}\big],$$

where $\mathcal{H}$, the Hamiltonian of the system, is introduced into our equation. Substituting into the time derivative of $G^{\alpha\beta}$ yields

$$\frac{d}{dt}\,G^{\alpha\beta}(\mathbf{Q},t) \;=\; -\,i\,\delta(t)\,\big\langle\big[\hat{S}^{\alpha}(\mathbf{Q},0),\, \hat{S}^{\beta}(-\mathbf{Q},0)\big]\big\rangle \;+\; \Theta(t)\,\big\langle\big[\big[\hat{S}^{\alpha}(\mathbf{Q},t),\, \mathcal{H}\big],\, \hat{S}^{\beta}(-\mathbf{Q},0)\big]\big\rangle.$$

Here, the delta-function term sets the initial condition at $t = 0$, while the second term captures how the Hamiltonian influences the spin operators and models the time evolution of the response. To transition to frequency space, we define the Fourier transform

$$G^{\alpha\beta}(\mathbf{Q},\omega) \;=\; \int_{-\infty}^{\infty} dt\;\, e^{\,i\,\omega\,t}\, G^{\alpha\beta}(\mathbf{Q},t).$$

Because $G^{\alpha\beta}(\mathbf{Q},t)$ is multiplied by $\Theta(t)$, the lower limit of integration is effectively 0 rather than $-\infty$. Upon performing this transform and rearranging, we obtain the standard frequency-domain equation of motion for the retarded Green's function:

$$\omega\, G^{\alpha\beta}(\mathbf{Q},\omega) \;=\; \big\langle\big[\hat{S}^{\alpha}(\mathbf{Q},0),\, \hat{S}^{\beta}(-\mathbf{Q},0)\big]\big\rangle \;+\; G\Big(\big[\hat{S}^{\alpha}(\mathbf{Q}),\, \mathcal{H}\big],\, \hat{S}^{\beta}(-\mathbf{Q}),\, \omega\Big) \qquad (3)$$

Physically, Eq. (3) encodes how the spin system evolves under the Hamiltonian $\mathcal{H}$. Interactions such as crystal-field effects or spin–orbit coupling enter via the commutator $[\hat{S}^{\alpha}(\mathbf{Q}),\mathcal{H}]$, showing how the Hamiltonian models the system's response. Finally, to connect this Green's function to the experimentally measurable spin structure factor, we

invoke the fluctuation–dissipation theorem [11]:

$$S^{\alpha\beta}(\mathbf{Q},\omega) \;=\; -\,\frac{1}{\pi}\,\frac{1}{1-e^{-\omega/(k_BT)}}\,\mathrm{Im}\,G^{\alpha\beta}(\mathbf{Q},\omega),$$

where k_B is Boltzmann's constant and T is the absolute temperature. This relation demonstrates that the imaginary part of the Green's function directly reflects the dissipation of energy within the spin system. Crucially, it also links the response measured in neutron scattering experiments to the fluctuations of the spins in the crystal (magnons), thereby making these fluctuations observable. Hence, in our next steps we must describe the relevant Hamiltonian for our system, which is fed back into the Green's function and is then used to model spin-wave excitations.

2.3 Magnetic Hamiltonian

Continuing onward, it is clear that the time evolution of our Green's function model is governed by the Hamiltonian of the system. Once a general model of the Hamiltonian has been established and a working Green's function formalism is in place, this analysis can be applied specifically to the structure of $CoTiO_3$. For the purposes of this paper, much of the mathematics, specifically the rigorous derivation of commutators and their relations, is sacrificed for general clarity. For the reader interested in these aspects of the mathematics, Buyers et al. and Popescu et al. [16, 17] outline all the steps. In this paper, the total magnetic Hamiltonian, $\mathcal{H}$, is written as [16]

$$\mathcal{H} = \mathcal{H}_{\mathrm{CF}} + \sum_{ij} J(ij)\hat{S}(i)\cdot\hat{S}(j), \tag{4}$$

where $J(ij)$ represents the exchange coupling constant between Co^{2+} ions at sites i and j, and $\mathcal{H}_{\mathrm{CF}}$ is the crystal field Hamiltonian. The second term describes the interaction between the spins of different Co^{2+} ions via the exchange coupling constant, with $J > 0$ for ferromagnetic and $J < 0$ for antiferromagnetic coupling. By expanding the dot product of the spin operators, the Hamiltonian can be partitioned into a single-ion part, $\mathcal{H}_1$, and an inter-ion part, $\mathcal{H}_2$ [16].

The single-ion Hamiltonian is defined as

$$\mathcal{H}_1 = \sum_i \mathcal{H}_{\mathrm{CF}}(i) + \sum_i S^z(i)\left(2\sum_j J(ij)\langle S^z(j)\rangle\right),$$

and the inter-ion Hamiltonian is given by

$$\mathcal{H}_2 = \sum_{ij} J(ij)S^z(i)\Big[S^z(j) - 2\langle S^z(j)\rangle\Big] + \frac{1}{2}\sum_{ij} J(ij)\Big[S^+(i)S^-(j) + S^+(i)S^-(j)\Big].$$

where $+$ and $-$ represent directions perpendicular to z. It is important to note that $\mathcal{H}_2$ represents the coupling between the single-ion excitations. In our approach, $\mathcal{H}_2$ is treated as a perturbation on top of the single-ion Hamiltonian, and its contributions are incorporated via the exchange term $J(\mathbf{Q})$.

2.3.1 Single-ion excitations ($\mathcal{H}_1$)

To address the single-ion Hamiltonian, $\mathcal{H}_1$, we first diagonalise it using ladder operators C_n and $C_m^\dagger$. The spin operators are expressed in terms of these ladder operators, which act on the eigenstates of the single-ion Hamiltonian [16]. These operators satisfy the commutation relation

$$[C_m^\dagger, C_n] = \delta_{mn}.$$

Thus, the single-ion Hamiltonian can be written as

$$\mathcal{H}_1 = \sum_i \sum_n \omega_n \, C_n^\dagger(i) C_n(i),$$

where ω_n represents the energy eigenvalues of the single-ion, and the operators $C_n^\dagger(i)$ and $C_n(i)$ respectively create and annihilate the corresponding eigenstates. In this representation, the spin operators $\hat{S}^z$, $\hat{S}^x$, and $\hat{S}^y$ are written as sums over these ladder operators:

$$\hat{S}^{+,-} = \sum_{mn} S_{mn}^{+,-} \, C_m^\dagger C_n, \quad \hat{S}^z = \sum_{mn} S_{mn}^z \, C_m^\dagger C_n,$$

where $S_{mn}^{+,-}$ and S_{mn}^z denote the matrix elements of the spin operators in the diagonal basis of the single-ion Hamiltonian.

After diagonalising the single-ion Hamiltonian $\mathcal{H}_1$, each ion is described by a set of quantised energy levels corresponding to its eigenstates. The ladder operators C_n and $C_n^\dagger$ are used to move the ion between these levels, and the resulting transitions represent the individual excitations of the ion. These excitations, which are characterized by energy differences $\omega_n - \omega_m$ and weighted by the thermal population differences $(f_m - f_n)$, form the basis of the single-ion susceptibility $g^{\alpha\beta}(\omega)$ [16], which will be discussed below.

2.3.2 Inter-ion excitations ($\mathcal{H}_2$)

Next, we consider the inter-ion interactions described by $\mathcal{H}_2$. To simplify the treatment of $\mathcal{H}_2$, we apply a mean-field approach and decouple products of spin operators on different sites using the random phase approximation (RPA) [11]. For instance, a term such as $\hat{S}^+(i)\hat{S}^+(j)$ is approximated by

$$\hat{S}^+(i)\hat{S}^+(j) \approx \langle \hat{S}^+(i) \rangle \, \hat{S}^+(j) + \hat{S}^+(i) \, \langle \hat{S}^+(j) \rangle - \langle \hat{S}^+(i) \rangle \, \langle \hat{S}^+(j) \rangle.$$

This decoupling reduces the complexity of the inter-ion Hamiltonian, allowing it to be treated as a perturbation on top of the diagonalised single-ion Hamiltonian. To capture the dynamics resulting from the coupling of multiple single-ion excitations, we introduce the inter-level susceptibility through the Green function of the ladder operators:

$$G^{\alpha\beta}(ij,\omega) = \sum_{mn} S_{mn}^\alpha \, \hat{G}^\beta(mn,ij,\omega),$$

where S_{mn}^α are the matrix elements of the spin operators and $\hat{G}^\beta(mn,ij,\omega)$ describes the propagation of excitations between levels m and n [16]. By applying the RPA and evaluating the commutators, we rotate $\mathcal{H}_2$ into the basis of $\mathcal{H}_1$, which has already been diagonalised. In this rotated basis, the commutator for the ladder operators simplifies to

$$(f_m(i) - f_n(i)) \, S_{nm}^\beta(j) \, \delta_{ij},$$

where $f_n(i)$ denotes the Boltzmann probability of state n. This expression emerges because, when the spin operators are expressed in the diagonal basis, the difference in the thermal occupation factors naturally appears. The δ_{ij} ensures that the contribution is confined to the same ion, reflecting the fact that the ladder operators act within a single-ion space. Summing the series of commutators under the RPA, the full Green's function in momentum space is expressed as:

$$G^{\alpha\beta}(\mathbf{Q},\omega) = g^{\alpha\beta}(\omega) + g^{\alpha+}(\omega)J(\mathbf{Q})\,G^{-\beta}(\mathbf{Q},\omega) + g^{\alpha-}(\omega)J(\mathbf{Q})\,G^{+\beta}(\mathbf{Q},\omega) + 2\,g^{\alpha z}(\omega)J(\mathbf{Q})\,G^{z\beta}(\mathbf{Q},\omega). \tag{5}$$

Here, the single-ion susceptibilities, which describe how a single-ion responds to external perturbations at a given frequency, are given by:

$$g^{\alpha\beta}(\omega) = \sum_{mn} \frac{S^{\alpha}_{mn}\,S^{\beta}_{mn}\,(f_m - f_n)}{\omega - \omega_n + \omega_m},$$

For high symmetry systems, this expression further simplifies into transverse and longitudinal components. The transverse Green's function is:

$$G^{+-}(\mathbf{Q},\omega) = \frac{g^{+-}(\omega)}{1 - J(\mathbf{Q})\,g^{+-}(\omega)},$$

and the longitudinal Green's function is:

$$G^{zz}(\mathbf{Q},\omega) = \frac{g^{zz}(\omega)}{1 - 2\,J(\mathbf{Q})\,g^{zz}(\omega)}.$$

These equations combine the single-ion dynamics and the inter-ion exchange effects to describe the collective spin-wave excitations in the system. Such excitations are then directly related to experimental observables, such as neutron scattering spectra, which can be plotted as dispersion relations [16].

3 Method: Linear Response Theory in the specific case of $CoTiO_3$

3.1 Structure and Crystal Electric Field

Now that we have the general building blocks, we must begin applying this method to $CoTiO_3$. Understanding the crystal structure and the associated crystal-field effects is the first step in our analysis, as these allow us to describe the relevant Hamiltonian for our compound. In the case of $CoTiO_3$, the structure is particularly interesting and complex.

$CoTiO_3$ consists of a stack of hexagonal lattices, as illustrated in Figure 1, with lattice parameters $a = b = 5.0662\,\mathring{A}$ and $c = 13.918\,\mathring{A}$. Notably, $CoTiO_3$ exhibits ferromagnetic ordering within each hexagonal plane (i.e. the spins of Co^{2+} are aligned within a plane), while the ordering between the planes is antiferromagnetic [18]. Consequently, the magnetic structure on each lattice is rotated by an angle $\theta = \pi$ relative to the lattices immediately above and below. Furthermore, as shown in Figure 3, to achieve a complete

honeycomb configuration, the site 2 Co^{2+} ions are assumed to lie approximately in the same plane as the ions at site 1, leading to a slight distortion of the ideal honeycomb structure.

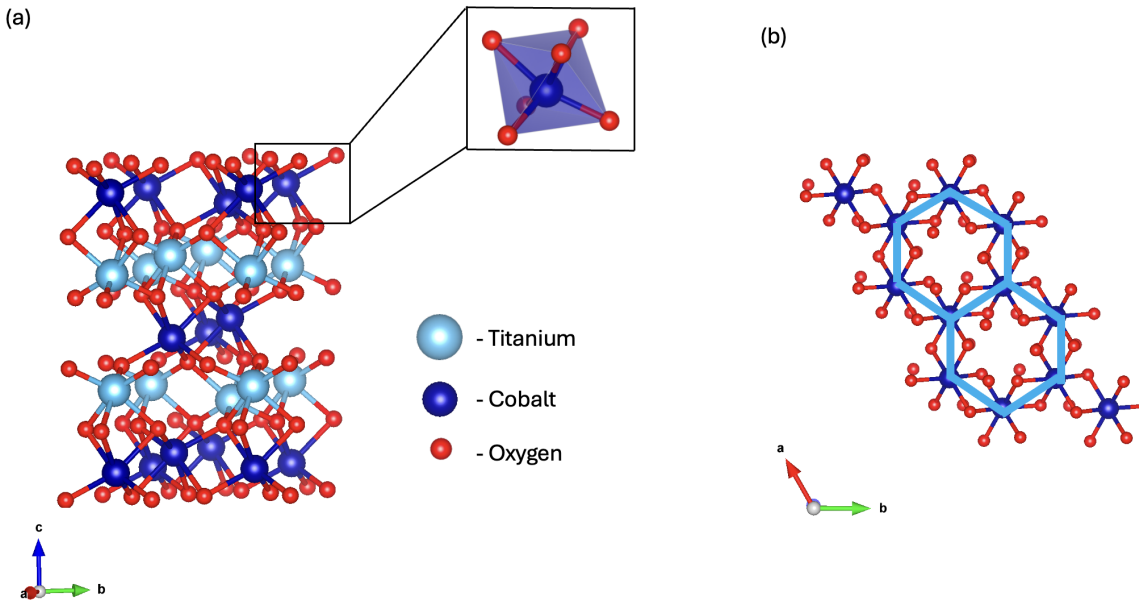

Figure 1: (a) Crystal structure of $CoTiO_3$ with the octahedral CoO_6 coordination. (b) In-plane structure of $CoTiO_3$ showing features of honeycomb with space group symmetry $R\bar{3}$.

The magnetic behaviour of $CoTiO_3$ is linked to the electronic configuration of the Co^{2+} ion, which has a $3d^7$ configuration. In an octahedral environment, as depicted in Figure 2 (a), the $3d$ orbitals split into two groups: the lower-energy t_{2g} orbitals (namely, d_{xy}, d_{xz}, and d_{yz}) and the higher-energy e_g orbitals (namely, d_{z^2} and $d_{x^2-y^2}$) [19]. This splitting, visualised in Figure 4 $(a), (b)$ has a splitting energy of approximately $10Dq \approx 1\,eV$ [20]. According to Hund's rule, the seven electrons fill these orbitals such that the spin configuration is $S = 3/2$, with two unpaired electrons in the e_g orbitals and one unpaired electron in the t_{2g} orbitals.

The situation is further complicated by the fact that the t_{2g} orbitals give rise to an effective orbital angular momentum $l = 1$, which results in a three-fold orbital degeneracy [19]. While the full $3d$ shell in the free-ion approximation has a total orbital angular momentum $L = 3$ (as per Hund's second rule), the presence of the crystal field reduces this to an effective $l = 1$ for the t_{2g} manifold. The initial 12-fold degeneracy (arising from 4 spin states and 3 orbital states) will now be lifted by the combined effects of perturbations on this $l = 1$ state, which we will now study.

In order to describe the single-ion physics in detail, and understand the splitting of these degenerate energy levels, we must decompose the single-ion Hamiltonian $\mathcal{H}_1$ into four components

$$\mathcal{H}_1 = \mathcal{H}_{\mathrm{CF}} + \mathcal{H}_{\mathrm{MF}} = \mathcal{H}_{\mathrm{CEF}} + \mathcal{H}_{\mathrm{SO}} + \mathcal{H}_{\mathrm{dis}} + \mathcal{H}_{\mathrm{MF}},$$

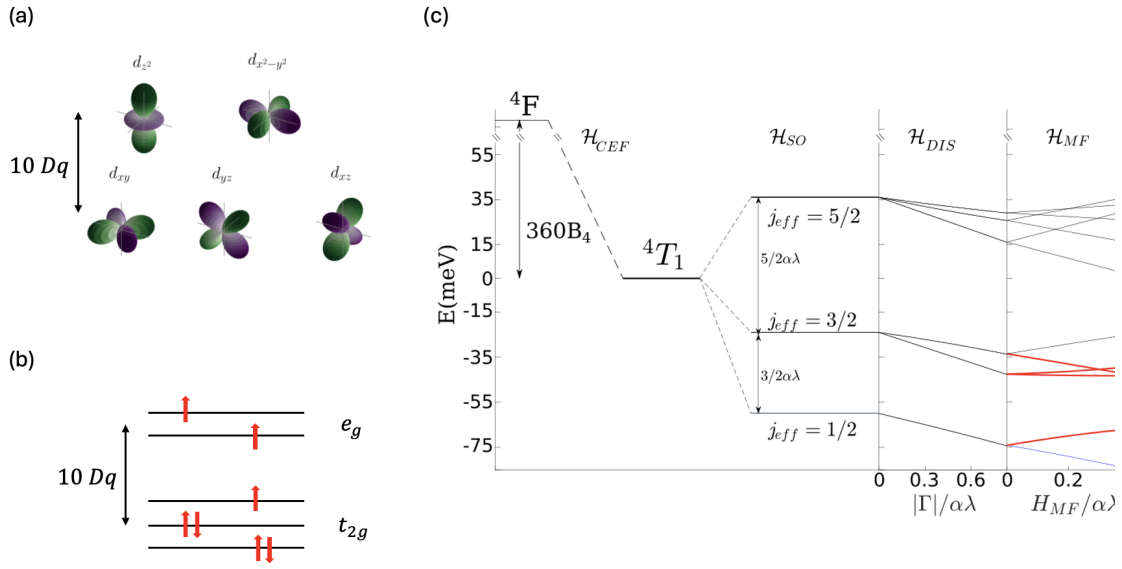

Figure 2: (a) Splitting of density plots of d-orbitals into crystal field levels [19]. (b) Crystal field levels of Co^{2+}, split by $10Dq \approx 1\,eV$. (c) Single-ion energy levels for Co^{2+} under the combined effects of spin–orbit coupling, structural distortion and the molecular field, in the presence of an applied crystal field.

where $\mathcal{H}_{\text{CEF}}$ represents the crystal electric field, $\mathcal{H}_{\text{SO}}$ the spin–orbit coupling, $\mathcal{H}_{\text{dis}}$ the distortion field, and $\mathcal{H}_{\text{MF}}$ the molecular field. Figure 2 (c) clearly shows how these contributions act to split the degenerate levels of Co^{2+}. In particular, since $\mathcal{H}_{\text{CEF}}$ is much smaller than the free-ion energy splitting [21], it can be treated as a perturbation on the free-ion ^4F state (with $L = 3$, $S = 3/2$ according to Hund's rules). As a result, $\mathcal{H}_{\text{CEF}}$ splits the ^4F state into two orbital triplets (with the ground state being $^4T_1$ and the excited state $^4T_2$) and an orbital singlet $^4A_2$. Due to the significant energy gap between $^4T_1$ and $^4T_2$, it is assumed that the magnetic properties of $CoTiO_3$ are predominantly determined by the $^4T_1$ ground state [22, 23], which is the $l = 1$ state previously mentioned above. Consequently, the terms $\mathcal{H}_{\text{SO}}$, $\mathcal{H}_{\text{dis}}$, and $\mathcal{H}_{\text{MF}}$ can be treated as perturbations on this ground state since $\mathcal{H}_{\text{CEF}} \gg \mathcal{H}_{\text{SO}} + \mathcal{H}_{\text{dis}} + \mathcal{H}_{\text{MF}}$.

3.2 Additional perturbations on $^4T_1$

The second key interaction to consider in $CoTiO_3$ is spin–orbit coupling, represented by the Hamiltonian

$$\hat{\mathcal{H}}_{\text{SO}} = \lambda \hat{L} \cdot \hat{S},$$

where λ is the spin–orbit coupling constant. This term introduces additional complexity to the magnetic behaviour, necessitating a projection from the initial $|L = 3, m_L\rangle$ basis onto a more restricted basis, $|l = 1, m_l\rangle = |\phi_{\text{CEF}}\rangle$. This approach effectively reduces the active basis to a subset that spans the crystal-field ground state, $^4T_1$, thereby simplifying calculations for the low-energy behaviour of the system. Abragam and Bleaney outline this basis projection process, achievable through representation theory [24]. In this work, however, an alternative method—employed by Satre et al. [11]—is applied: a matrix representation of the angular momentum operators is used to derive a transformation matrix C that maps from the $|L = 3, m_L\rangle$ basis to the crystal-field basis $|\phi_{\text{CEF}}\rangle$ [25, 26].

This matrix C, with columns corresponding to eigenvectors of $\hat{\mathcal{H}}_{\text{CEF}}$ ordered by increasing energy eigenvalues, allows rotation from the $|L = 3, m_L\rangle$ basis to the $|\phi_{\text{CEF}}\rangle$ basis, expressed as [11]

$$\hat{O}|\phi_{\text{CEF}}\rangle = C^{-1}\hat{O}|L, m_L\rangle\, C \quad \text{for any operator } \hat{O}.$$

For the $\hat{L}_z$ operator, this transformation gives a matrix in the $|\phi_{\text{CEF}}\rangle$ basis whose top 3×3 block aligns with the $\hat{L}_z$ operator in the reduced $|l = 1, m_l\rangle$ basis, confirming that the effective orbital angular momentum is reduced to $l = 1$. This outcome introduces a scaling factor $\alpha = -3/2$, which modifies the spin–orbit Hamiltonian to [11]:

$$\hat{\mathcal{H}}_{\text{SO}} = \alpha\lambda\hat{l} \cdot \hat{S},$$

where $\hat{l}$ now represents the effective angular momentum operator within the reduced $|l = 1, m_l\rangle$ basis.

Our distortion Hamiltonian for a Co^{2+} octahedral structure can be approximated as [27]

$$\hat{\mathcal{H}}_{dis} = \Gamma\left(\hat{l}_z^2 - \frac{2}{3}\right),$$

which plays a modest role in splitting the non-degenerate $j_{\text{eff}} = \frac{1}{2}, \frac{3}{2}, \frac{5}{2}$ levels; however, it is significant as it represents a fixed parameter, Γ, based on observations of the splitting of the $j_{\text{eff}} = 3/2$ levels in $Na_2BaCo(PO_4)_2$ [17]. Finally, the molecular field Hamiltonian, $\hat{\mathcal{H}}_{\text{MF}}$, acts as a Zeeman term, splitting the degenerate j_{eff} levels. This term is primarily defined via nearest-neighbour interactions ($\mathcal{J}_1$) and is given by [11]:

$$\hat{\mathcal{H}}_{\text{MF}} = \sum_i h_{\text{MF}}(i)S_z = 2z_1\mathcal{J}_1\langle\hat{S}_z\rangle\hat{S}_z.$$

Having now incorporated the perturbative effects of spin–orbit coupling, structural distortions, and the molecular field into our description of the ${}^4T_1$ ground state, we have assembled a complete single-ion Hamiltonian for $CoTiO_3$. In the next step, we will define our $\mathcal{J}(\mathbf{Q})$ to account for the inter-ion interactions, while recognising that the specific magnetic structure of $CoTiO_3$ brings additional complications. Once these issues are addressed and the inter-ion coupling is properly incorporated, we will obtain a complete Green's function. Through the fluctuation–dissipation theorem, this Green's function gives the spin structure factor as we explained above, which in turn allows us to calculate the neutron scattering cross section and plot the spin fluctuations as dispersion relations. This will form the foundation for our later discussion on bond-dependent exchange interactions and the resulting anisotropic magnetic dynamics.

3.3 $\mathcal{J}(\mathbf{Q})$ and the need for a Rotating Frame

Thus far, we have defined our single-ion Hamiltonian and described how it is diagonalised for use in our Green's function formalism. However, to complete our theoretical description of the magnetic dynamics in $CoTiO_3$, we must now incorporate the exchange interactions between Co^{2+} ions. This is encapsulated in the momentum-dependent exchange function $\mathcal{J}(\mathbf{Q})$, defined as [11]

$$\mathcal{J}(\mathbf{Q}) = \frac{1}{N}\sum_{mn}\mathcal{J}_{mn}\, e^{-i\mathbf{Q}\cdot(\mathbf{r}_m - \mathbf{r}_n)}.$$

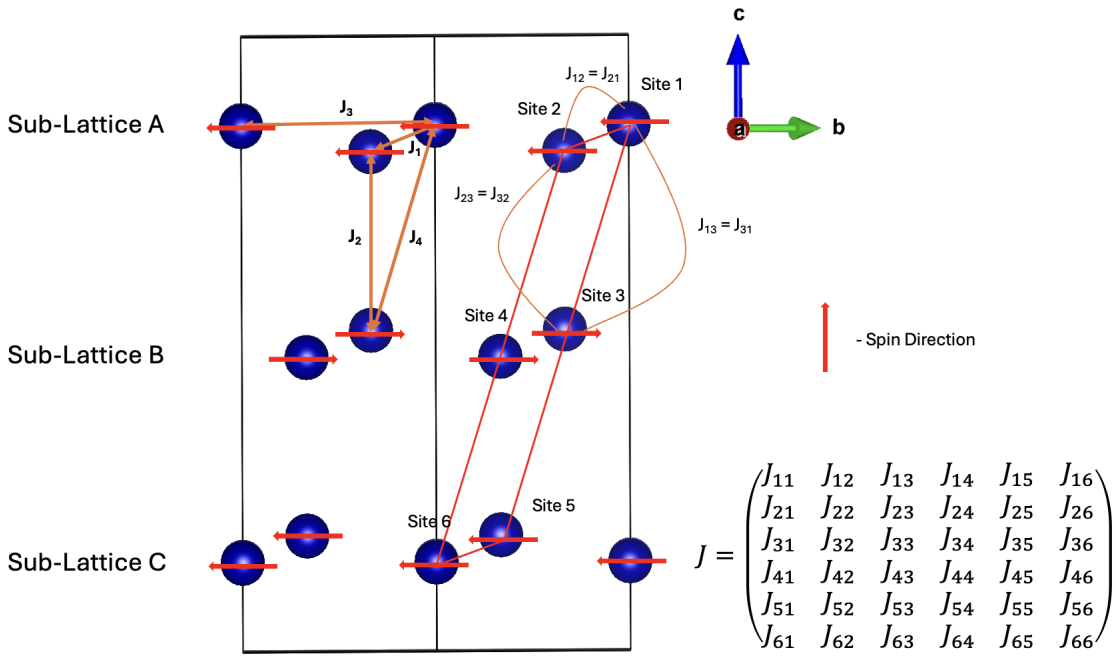

Figure 3: Figure showing the six site *spin unit cell* considered when modeling $CoTiO_3$. As examples, the exchange interactions between site 1 and 2, sites 1 and 3 and sites 2 and 3 are pictorially shown. Further, the anti-ferromagnetic out-of-plane structure is shown, with sites 3 and 4 having spin directions rotated $\theta = \pi$ to the sublattices above and below it. Finally, the matrix J involving all the interactions in the spin unit cell is written

where $r_m - r_n$ is the displacement between the interacting sites. Incorporating $\mathcal{J}(\mathbf{Q})$ into the Green's function allows us to use its imaginary part to model the spin structure factor, which in turn provides the dispersion relations of the magnetic excitations. However, $CoTiO_3$ presents additional challenges due to its complex magnetic ordering.

To capture all relevant physics, we restrict the exchange interactions to a defined region known as the *spin unit cell* [28]. In $CoTiO_3$, the spin unit cell comprises six sites across three Co^{2+} sub-lattices, as illustrated in Figure 3. Owing to the out-of-plane antiferromagnetic ordering, the magnetic dipoles of sites 1, 2, 5, and 6 are oriented at an angle $\theta = \pi$ relative to those in the immediately adjacent layers (sites 3 and 4) [5]. To deal with this, the work of Haraldsen et al. on a spin rotation technique for non-collinear magnetic systems is used [29].

3.3.1 Step 1: Intra-Cell Rotation within the "Spin Unit Cell"

Since sites 1, 2, 5, and 6 are aligned in one direction while sites 3 and 4 are rotated by π, we first apply an intra-cell rotation matrix X to align all spins within the unit cell onto a common axis. This is defined as [28]:

$$X = \begin{pmatrix} U(0) & 0 & 0 & 0 & 0 & 0 \\ 0 & U(0) & 0 & 0 & 0 & 0 \\ 0 & 0 & U(\pi) & 0 & 0 & 0 \\ 0 & 0 & 0 & U(\pi) & 0 & 0 \\ 0 & 0 & 0 & 0 & U(0) & 0 \\ 0 & 0 & 0 & 0 & 0 & U(0) \end{pmatrix},$$

where $U(0)$ leaves the spin orientation unchanged for sites 1, 2, 5, and 6, while $U(\pi)$ rotates the spins at sites 3 and 4 by π in the ab-plane. Explicitly, the rotation matrix $U(\theta)$ is given by [28]:

$$U(\theta) = \begin{pmatrix} 0 & \sin\theta & \cos\theta \\ 0 & -\cos\theta & \sin\theta \\ 1 & 0 & 0 \end{pmatrix}.$$

This intra-cell rotation ensures that all spins are brought into a common local frame, which is essential for the coherent treatment of exchange interactions.

3.3.2 Step 2: Rotation of the Entire Unit Cell

After aligning the spins within the unit cell, we address the inter-cell variation by rotating the entire unit cell. This is necessary because in $CoTiO_3$, the local orientation of the spins varies from one unit cell to the next. Physically, this step accounts for the incommensurate nature of the magnetic structure. We define the unit cell rotation by a matrix R_i that is related to the magnetic ordering wavevector $\mathbf{k}$, which represents the magnetic ordering vector that captures the periodicity of the magnetic structure, and a common rotation axis $\mathbf{n}$ using Rodrigues' rotation formula [28]:

$$R_i = e^{i\mathbf{k}\cdot\mathbf{r}_i}\Phi + e^{-i\mathbf{k}\cdot\mathbf{r}_i}\Phi^* + \mathbf{n}\mathbf{n}^T,$$

where

$$\Phi = \frac{1}{2}\left(\mathbf{1} - \mathbf{n}\mathbf{n}^T - i[\mathbf{n}]_\times\right),$$

and $[\mathbf{n}]_\times$ is the skew-symmetric matrix of $\mathbf{n}$. This rotation matrix transforms the spin components from the local reference frame to a global frame aligned with the magnetic ordering direction.

3.3.3 Green's Function in the Rotating Frame and Final Transformation

In the rotating frame, the Green's function $\tilde{G}(\mathbf{Q},\omega)$ satisfies the Dyson equation [28]:

$$\tilde{G}(\mathbf{Q},\omega) = g(\omega) + g(\omega)\tilde{\mathcal{J}}(\mathbf{Q})\tilde{G}(\mathbf{Q},\omega),$$

where the rotated exchange matrix $\tilde{\mathcal{J}}(\mathbf{q})$ is defined as

$$\tilde{\mathcal{J}}(\mathbf{Q}) = \mathcal{J}(\mathbf{Q}+\mathbf{k})\Phi + \mathcal{J}(\mathbf{Q}-\mathbf{k})\Phi^* + \mathcal{J}(\mathbf{Q})\,\mathbf{n}\mathbf{n}^T.$$

Finally, to express the Green's function in the laboratory frame, we combine the effects of the intra-cell rotation X and the unit-cell rotation R_i to obtain

$$G(\mathbf{Q},\omega) = R_i X\,\tilde{G}(\mathbf{Q},\omega)\,X^T R_i^T + R_i X\,\tilde{G}(\mathbf{Q}+\mathbf{k},\omega)\,X^T R_i^T + R_i^* X\,\tilde{G}(\mathbf{Q}-\mathbf{k},\omega)\,X^T R_i^{*T}.$$

In this expression, R_i is the unit cell rotation defined by Rodrigues' formula, and the matrices X and X^T account for the intra-cell alignment. The terms $\tilde{G}(\mathbf{Q},\omega)$ and its shifted forms $\tilde{G}(\mathbf{Q}\pm\mathbf{k},\omega)$ are the Green's functions in the rotating frame. This final expression encapsulates all necessary rotations and transformations to compute the Green's function $G(\mathbf{Q},\omega)$ in the laboratory frame for the specific magnetic structure of $CoTiO_3$.

With these building blocks in place, we are now equipped to model the theoretical response. Our ultimate goal was to compute the neutron scattering cross section using the Green's function. It was first essential to complete our analysis of the single-ion Hamiltonian and its perturbations. Only once the exchange interactions are fully incorporated via $\mathcal{J}(\mathbf{Q})$ and the rotating frame was established can we now calculate the dynamic response given by the Green's function. In the low-temperature limit (T $\to$ 0 K), the neutron response is given by [11]

$$S(\mathbf{Q},\omega) \underset{\sim}{\propto} -f^2(\mathbf{Q})\,\mathcal{IG}(\mathbf{Q},\omega),$$

which is a calculable quantity once our Green's function is transformed from the rotating frame back to the laboratory frame.

4 Results and Discussion: Dimers and Bond-Dependent exchange

4.1 Initial Findings

Due to a lack of access to direct experimental data, much of our analysis is based on a qualitative comparison with results reported in the literature [5, 6, 19]. Despite these limitations, our theoretical model successfully captures many of the essential features of the observed magnon spectrum in $CoTiO_3$. In particular, the model reproduces a key characteristic identified in previous studies: the presence of a *Dirac cone*. This Dirac cone arises from the linear crossing of two magnon bands at discrete momentum points, which is a direct consequence of the underlying honeycomb lattice symmetry and the specific exchange interactions that govern the system [5].

In our calculated spectra, the Dirac cone feature is observed prominently along the $[H+2/3, H-2/3]$ direction. As indicated by the yellow arrow in Figure 4, the magnon bands disperse linearly away from the crossing point, forming a conical structure that is characteristic of massless Dirac quasiparticles. This observation implies that the magnons in $CoTiO_3$ behave as relativistic particles, analogous to the electrons in graphene, but with Bose-Einstein statistics [5].

However, while the overall dispersion trends are well captured, our calculations along multiple momentum paths—particularly those illustrated in Figure 5—reveal an important discrepancy. Specifically, the model lacks the necessary enhancement of the exchange interaction near $[1, 0, 1/2]$. Here, the dispersion appears to be missing a mode that extends to approximately 2 meV. This suggests that the current model, which does not include bond-dependent exchange interactions, is insufficient to break the degeneracy of the existing modes. In order to fully capture the observed spin-wave dynamics, an additional interaction term—one that enhances the dispersion of a specific mode and lowers

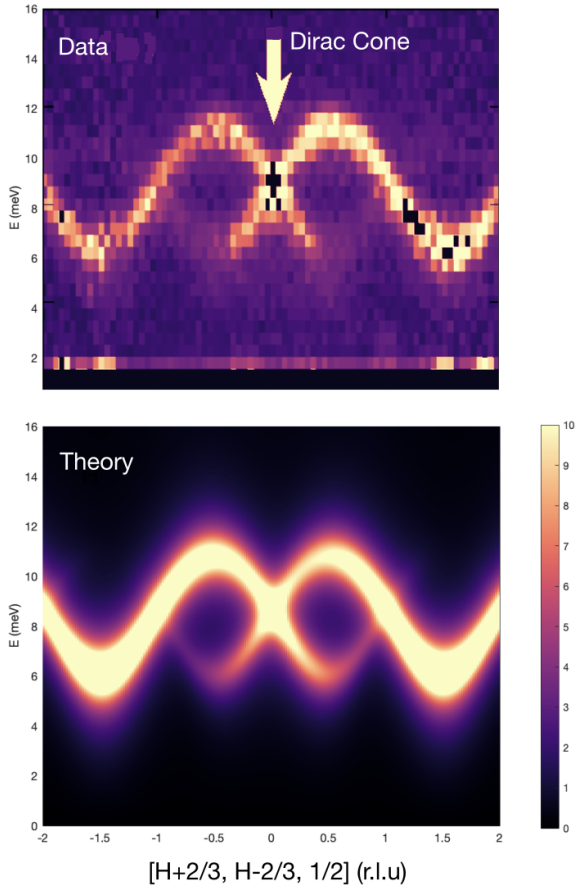

Figure 4: Comparison of experimental (top) [5] and theoretical (bottom) spectra along the $[H + 2/3, H - 2/3]$ direction, showing the presence of a Dirac cone. The linear crossing of magnon bands at the nodal point confirms the relativistic nature of magnons in $CoTiO_3$.

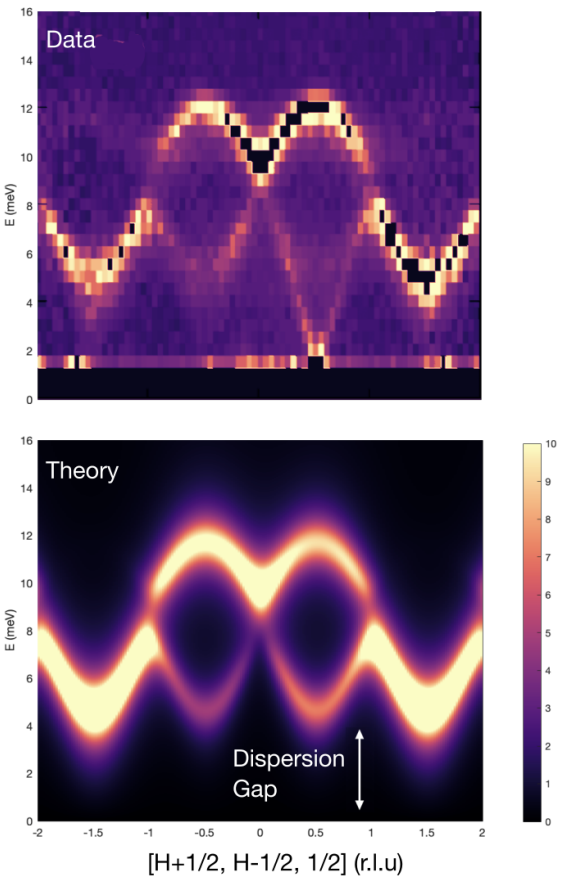

Figure 5: Spin-wave dispersion along the measured momentum paths, comparing experimental (top) [5] and theoretical (bottom) spectra. The missing enhancement of J_4 is evident, as the theoretical model lacks the necessary enhancement and fails to capture this feature near the high-symmetry points.

its energy—is required.

These initial findings underscore the need to refine our original theoretical framework by incorporating bond-dependent exchange interactions. In the following sections, we will explore this refinement in greater detail. We will demonstrate how the inclusion of an enhanced J_4 term, arising from dimerisation, leads to a more accurate description of the magnetic excitations in $CoTiO_3$. This refined model not only better reproduces the dispersion features but also provides insight into the underlying physics of the crystal.

4.2 The need for bond-dependent exchange

From above, it was clear that the dispersion near $[1, 0, 1/2]$ is missing an excitation mode that should extend to approximately 2 meV. This observation implies that the standard isotropic exchange interaction is insufficient to fully describe the magnetic excitations in this system. To resolve this issue, we turn to the concept of bond-dependent exchange,

which naturally introduces an anisotropy that can break the degeneracy of the modes and reproduce the full experimental dispersion.

4.2.1 Resonating Valence Bond Theory

To physically explain the required enhancement of J_4 (which we will see below is necessary to reproduce the dispersion relation), we consider the formation of quantum dimers as described by resonating valence bond (RVB) theory [4]. RVB theory states that in strongly correlated systems the ground state is not a fixed arrangement of spins but rather a superposition of many dimer configurations. In this picture, the valence bonds—i.e. the spin-singlet pairs—resonate among different configurations, thereby lowering the overall energy and enhancing quantum fluctuations. Though the traditional RVB framework highlights a fully delocalised network of singlets that can suppress long-range order, here we concentrate on the local dimerisation aspect, wherein certain exchange pathways form singlet pairs and acquire an enhanced coupling.

In our system, we postulate that the enhanced J_4 exchange is a result of dimer formation along specific crystallographic directions. This selective dimerisation modifies the local exchange interactions and leads to the spectral features observed experimentally. Notably, while the classical Néel state is described by a staggered spin arrangement,

$$|\psi_{\text{Néel}}\rangle = \prod_{i\in A, j\in B} |\uparrow_i\downarrow_j\rangle,$$

which minimises the exchange energy uniformly, the formation of dimers in the J_4 direction results in a locally bound singlet state as is schematically captured in Figure 6:

$$|\psi_{\text{Singlet}}\rangle = \frac{1}{\sqrt{2}}\left(|\uparrow\downarrow\rangle - |\downarrow\uparrow\rangle\right).$$

Before we show that a singlet state along J_4 is energetically favourable to the Néel state, we must justify why dimer formation occurs in the J_4 direction. Importantly, we do not observe the formation of in-plane ferromagnetic dimers (e.g. via the J_1 exchange) because such a dimer would be a triplet state, leading to a threefold degeneracy. This degeneracy could trigger a spin Jahn-Teller effect [30], resulting in structural distortions that have not been reported; hence, it is primarily the second-nearest out-of-plane exchange interactions that undergo this dimerisation.

4.2.2 Energy Comparison Between the Néel State and Singlet State

To quantitatively justify the energetic favourability of the singlet dimer state over the classical Néel state, we calculate their energies using the Heisenberg exchange model [4]. For antiferromagnetic interactions ($J > 0$), the energy per bond in the classical Néel state is given by:

$$E_{\text{Néel}} = -\frac{1}{4}J.$$

In contrast, the energy for a singlet state, derived from the action of the exchange Hamiltonian on the singlet wavefunction, is:

$$H|\psi_{\text{Singlet}}\rangle = J\,\hat{S}(i)\cdot\hat{S}(j)|\psi_{\text{Singlet}}\rangle.$$

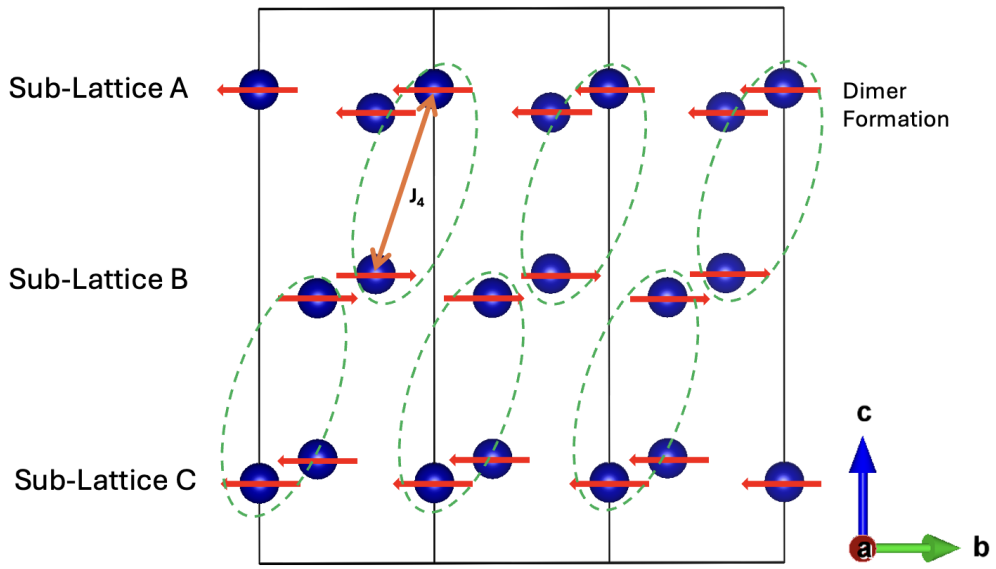

Figure 6: Illustration of dimer formation in $CoTiO_3$ driven by enhanced out-of-plane exchange interaction J_4. The system exhibits in-plane ferromagnetic ordering (red arrows) within each sublattice, while interlayer coupling leads to the formation of singlet dimers (green dashed ovals) along the enhanced exchange direction.

Using the identity

$$\hat{S}(i) \cdot \hat{S}(j) = \frac{1}{2}\left(\hat{S}^2 - \hat{S}(i)^2 - \hat{S}(j)^2\right),$$

and recognising that for a singlet $S^2 = 0$ and $\hat{S}(i)^2 = \hat{S}(j)^2 = \frac{3}{4}$, we obtain:

$$E_{\text{Singlet}} = -\frac{3}{4}J.$$

Thus, the energy difference per bond is:

$$E_{\text{Singlet}} - E_{\text{Néel}} = -\frac{3}{4}J + \frac{1}{4}J = -\frac{1}{2}J,$$

demonstrating that the singlet state is lower in energy by $\frac{1}{2}J$ per bond. However, in a crystal with uniform symmetry, all exchange pathways are equivalent and hence there exists no reason for why any one exchange pathway should be enhanced. Only when structural distortions break this symmetry can dimers form selectively, highlighting the need for such distortions in the $CoTiO_3$ structure.

4.2.3 Lattice Distortions and the Breaking of Exchange Equivalence

At high temperatures, $CoTiO_3$ crystallises in the space group $R\bar{3}$ (No. 148) [31], characterised by a threefold rotational axis and the $\bar{3}$ rotoinversion symmetry. Within this symmetry, all in-plane bonds are strictly equivalent, and so are certain out-of-plane bonds. This would mean that exchange equivalence is enforced and there should be no preferential dimer formation along specific directions.

However, recent high-resolution diffraction and thermal expansion measurements by Hoffmann et al. [9], demonstrate that upon cooling $CoTiO_3$ below its Néel temperature T_N, it undergoes strong magnetoelastic distortions: they observed anomalous shifts in the lattice parameters (particularly along the c axis) and changes in Bragg intensities. Although their refinements remain consistent with an overall $R\bar{3}$ description, the effective equivalence of certain out-of-plane bonds is lost once magnetic order sets in. In other words, the equivalent exchange condition that would be imposed by a $R\bar{3}$ crystal free of internal strain is no longer strictly maintained in the magnetically ordered phase. This provides an explanation for the anisotropic exchange, especially for the out-of-plane coupling J_4, which can become enhanced relative to other nearest- or next-nearest-neighbour interactions.

4.2.4 Modelling Anisotropic Exchange

To incorporate the selective enhancement of J_4 due to dimer formation, we introduce a crude Gaussian decay model. This approach modulates the exchange interaction J_4 as a function of momentum $\mathbf{Q}$ to reflect the anisotropic enhancement observed experimentally. Mathematically, the modulation function $M(\mathbf{Q})$ is defined as

$$J_4 = J_4 + J_4 \cdot M(\mathbf{Q}),$$

where

$$M(\mathbf{Q}) = A \cdot \exp\left(-\frac{d^2_{\text{centre}}}{2\sigma^2}\right),$$

and d_{centre} is the radial distance in the H-K plane from the enhancement centre at $(H_{\text{centre}}, K_{\text{centre}}, L_{\text{centre}}) = (1, 1, 3/2)$ or $(1, 0, 1/2)$. This formulation ensures that the exchange interaction is maximised at these points and decays smoothly away from this point, thereby capturing the bond-dependent nature of the exchange.

Together, these demonstrate that by including bond-dependent exchange through an enhanced J_4, our theoretical model can account for the missing dispersion mode and more accurately reproduce the experimental magnon spectrum. This refined understanding will serve as the foundation for our subsequent analysis of the anisotropic magnetic dynamics in $CoTiO_3$.

4.3 The Anisotropic Exchange Model and its physical implications

Upon introducing the Gaussian enhancement of J_4 to account for bond-dependent exchange, our theoretical model now closely reproduces the experimental dispersion near the critical region, as clearly illustrated in Figure 7 (a). In this region, the enhanced J_4 coupling acts to significantly lower the magnon energy, thereby lifting the degeneracy of the higher energy mode that was previously unresolved in the isotropic model.

We can extend our discussion to the higher energy data by examining the first spin–orbit transition, as shown in Figure 7 (b). The energy scale for this excitation is principally defined by the spin–orbit Hamiltonian, $\mathcal{H}_{\text{SO}}$, and the distortion term, $\mathcal{H}_{\text{dis}}$, which in turn set the parameters λ and Γ in our Green's function response model. In the experimental data, the constant momentum cuts along the specified path exhibit a dispersion

from approximately 32 meV to 24 meV. Initially, the isotropic exchange model provided reasonable agreement with the data; however, it failed to capture the 24 meV minimum along the $[1, 1, 3/2]$ direction. This was rectified by incorporating the enhanced J_4 term via bond-dependent exchange, which effectively reproduces the observed reduction in magnon energy.

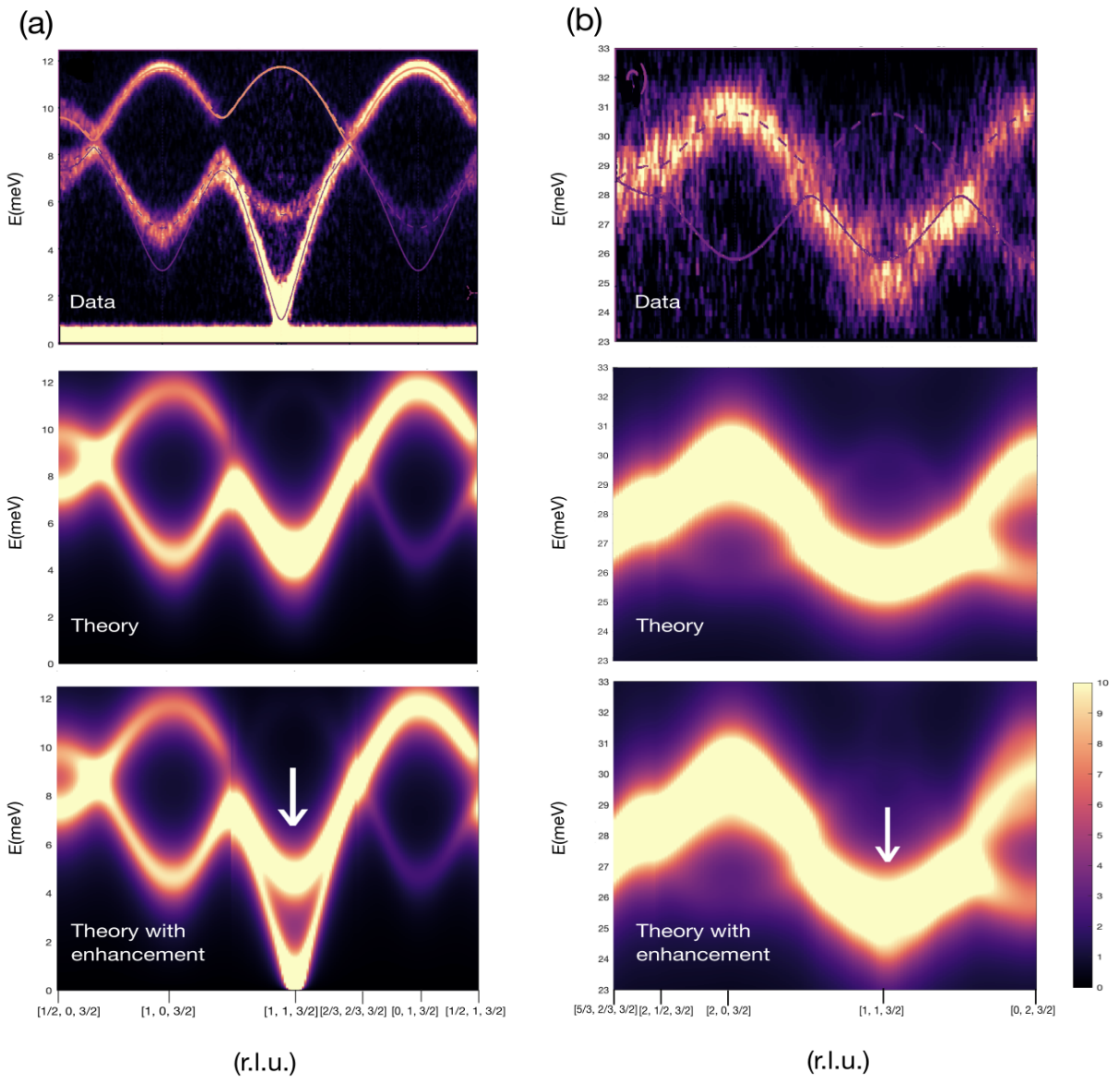

Figure 7: (a) Comparison of experimental [6] and theoretical spectra in plane, showing that the enhancement of J_4 as a consequence of dimerisation leads to the correct enhanced dispersion and splitting of spin-wave modes, mainly around $[1, 1, 3/2]$. (b) Spin-orbit dispersion along the measured momentum paths, comparing experimental [6] and theoretical spectra with enhancement replicating the data more accurately.

Table 1 summarises the parameters used in our calculations. These parameters are in strong agreement with the expected single-ion energy splittings for the spin–orbit levels in $CoTiO_3$, and, although they were obtained through qualitative comparison, they are consistent with physical constraints imposed by our model. For example, the dependence

between h_{MF} and J_1 in the molecular field Hamiltonian, given by $h_{\mathrm{MF}} = 2z_1 J_1 S(S+1)$, provides an internal consistency check. Our calculated value $2z_1 J_1 \langle \hat{S}_z \rangle = 3.75 \pm 0.2$ meV is in close agreement with the required molecular field of 4.0 ± 0.2 meV. Also, a strong molecular field of 4.0 meV is expected for a commensurate in-plane magnetic ordering in $CoTiO_3$.

$CoTiO_3$ Green's Function Model Parameters

Parameter	Value
α	$-3/2$
λ	-12.75 ± 0.05 meV
Γ	-12.0 ± 0.5 meV
h_{MF}	4.0 ± 0.2 meV
J_1	-0.21 ± 0.02 meV
ω (broadening)	0.9 ± 0.1 meV
J_4	0.008 ± 0.002 meV
$A(J_1)$	0.50 ± 0.01
$A(J_4)$	9.5 ± 0.1
σ	1.0 ± 0.5

Table 1: Model parameters used in the calculation

Furthermore, the large broadening parameter, ω, arises from the limited resolution of the experimental dispersions, leading to a more smeared out dispersion. Both α and λ are fixed parameters, determined by the single-ion physics of Co^{2+} [20, 32], while the distortion factor Γ is based on previous studies on $Na_2BaCo(PO_4)_2$ [17]—although slightly higher in our case due to the greater octahedral distortions (ranging from 88.99° to 101.62°).

The Gaussian decay model further supports the dimerisation process, as it shows that the enhancement in J_4 is significant only along specific directions where dimers form (increasing up to $10.5\,J_4$ at the enhancement point) while J_4 is effectively zero elsewhere. In contrast, the enhancement in J_1 (the in-plane exchange) is modest, increasing to about $1.5\,J_1$, and is therefore of secondary importance compared to J_4. These observations validate our physical model and provide strong evidence for bond-dependent exchange and dimer formation in $CoTiO_3$.

An additional test of the model's physicality is the calculation of the Curie–Weiss (CW) temperature. With the CW temperature reported as ≈ 15 K from multiple sources [18, 33, 34], and recognizing that a factor of $\frac{1}{2}$ is introduced in our derivation, we can compute the CW temperature using [35]

$$\theta_{\mathrm{CW}} = -\frac{1}{3k_B} S(S+1) \sum_i z_i J_i,$$

where z_i is the number of relevant nearest neighbours (specifically, the fourth nearest in the case of J_4). This yields $\theta_{\mathrm{CW}} = 1.5$ meV (≈ 17.4 K), in strong agreement with experiment. Discrepancies when using enhanced J's indicate that the simple free-spin assumption for susceptibility is insufficient once dimerisation sets in, corroborating the need for our dimerised framework.

Stone et al. [36] further explored this phenomenon by demonstrating that a frustrated spin–singlet phase results in an exponential suppression of the susceptibility at low temperatures, thereby deviating markedly from the predictions of the Curie–Weiss law. This observation is also seen in studies on spin–Peierls systems, where Hase et al. [37] showed that the onset of dimerisation leads to a rapid, exponential drop in susceptibility below the transition temperature. Moreover, Kageyama et al. [38] provided compelling evidence in the two-dimensional spin-gap system $SrCu_2(BO_3)_2$ that when an exact dimer ground state emerges, a quantised magnetisation plateaux is observed. Together, these experimental and theoretical findings indicate that once dimerisation occurs, the magnetic system deviates significantly from the conventional free-spin picture underlying usual susceptibility and CW calculations, thus necessitating a shift from an independent spin model to one based on a dimerised framework.

In summary, the refined anisotropic exchange model, incorporating an enhanced J_4 via bond-dependent exchange, not only reproduces the observed dispersion features in $CoTiO_3$ but also provides a deeper physical understanding of the underlying magnetic interactions. This treatment can form a basis for the subsequent discussion of anisotropic magnetic dynamics and their implications for the system's overall behaviour.

5 Conclusion and Future Research

In this study, we have explored the bond-dependent exchange in $CoTiO_3$ by modelling its magnon dispersions using a Green's function approach. Our analysis reveals that a simple isotropic bond model reproduces some of the fundamental features observed in the experimental data—such as the emergence of a Dirac cone along certain momentum directions—but fails to capture the enhanced dispersions observed near the $[1, 1, 3/2]$ and $[1, 0, 1/2]$ directions. By introducing an anisotropic enhancement of the exchange parameter J_4 via a Gaussian decay modulation, we have successfully reproduced these enhanced dispersions. This refinement not only validates our theoretical framework but also provides deeper insight into the role of bond-dependent exchange interactions in governing the magnetic behaviour of $CoTiO_3$.

The physical justification for this enhancement is supported by resonating valence bond (RVB) theory, which states that the formation of quantum dimers lowers the system's overall energy compared to the conventional Néel state. Furthermore, our work highlights the critical role of lattice distortions in breaking exchange equivalence in $CoTiO_3$ and enabling selective dimerisation. This structural transition is key to understanding the observed bond-dependent exchange effects.

Our Green's function formalism has enabled us to accurately model both the low-energy spin waves and the higher-energy spin–orbit excitations, with the parameters derived being in strong agreement with independent physical constraints, such as the Curie–Weiss temperature, and in internal consistency between the molecular field and the exchange interactions. However, our analysis is not without limitations. Access to more comprehensive, high-resolution neutron scattering data would allow us to further refine our model—particularly in resolving discrepancies in intensity of the dispersion across different momentum directions.

Moreover, investigations into the exact formation and dynamics of the dimerised phase, which we simply propose as a static one, may provide reasons for why enhancement only occurs at specific crystallographic points. Studies of acoustic phonon anomalies linked to spin Jahn–Teller effects could provide further insights into why J_1 was also slightly enhanced. Such studies would not only validate the present theoretical framework but also advance our understanding of unconventional magnetic behaviour in transition metal compounds, and potentially lead to a greater understanding of spin-liquid candidates in general.

References

1. Liu, H., Chaloupka, J. & Khaliullin, G. Kitaev spin liquid in 3 d transition metal compounds. *Physical Review Letters* **125,** 047201 (2020).
2. Liu, H. & Khaliullin, G. Pseudospin exchange interactions in d 7 cobalt compounds: Possible realization of the Kitaev model. *Physical Review B* **97,** 014407 (2018).
3. Sano, R., Kato, Y. & Motome, Y. Kitaev-Heisenberg Hamiltonian for high-spin d 7 Mott insulators. *Physical Review B* **97,** 014408 (2018).
4. Anderson, P. W. Resonating valence bonds: A new kind of insulator? *Materials Research Bulletin* **8,** 153–160 (1973).
5. Yuan, B. *et al.* Field-dependent magnons in the honeycomb antiferromagnet CoTiO 3. *Physical Review B* **109,** 174440 (2024).
6. Elliot, M. *et al.* Order-by-disorder from bond-dependent exchange and intensity signature of nodal quasiparticles in a honeycomb cobaltate. *Nature Communications* **12,** 3936 (2021).
7. Kimura, T. Spiral magnets as magnetoelectrics. *Annu. Rev. Mater. Res.* **37,** 387–413 (2007).
8. Tokura, Y. & Seki, S. Multiferroics with spiral spin orders. *Advanced materials* **22,** 1554–1565 (2010).
9. Hoffmann, M. *et al.* Magnetic phase diagram, magnetoelastic coupling, and Grüneisen scaling in CoTiO 3. *Physical Review B* **104,** 014429 (2021).
10. Shirane, G., Shapiro, S. M. & Tranquada, J. M. *Neutron scattering with a triple-axis spectrometer: basic techniques* (Cambridge University Press, 2002).
11. Sarte, P. *et al.* Spin-orbit excitons in CoO. *Physical Review B* **100,** 075143 (2019).
12. Kernavanois, N., Ressouche, E., Brown, P., Henry, J. & Lelievre-Berna, E. Magnetization distribution in paramagnetic CoO: a polarized neutron diffraction study. *Journal of Physics: Condensed Matter* **15,** 3433 (2003).
13. Kernavanois, N., Ressouche, E., Brown, P., Henry, J. & Lelievre-Berna, E. Magnetization distribution in paramagnetic nickel and cobalt oxides. *Physica B: Condensed Matter* **350,** E265–E267 (2004).
14. Prince, E. *International Tables for Crystallography, Volume C: Mathematical, physical and chemical tables* (Springer Science & Business Media, 2004).
15. Zhu, Y. *Modern techniques for characterizing magnetic materials* (Springer, 2005).

16. Buyers, W., Holden, T. & Perreault, A. Temperature dependence of magnetic excitations in singlet-ground-state systems. II. Excited-state spin waves near the Curie temperature in Pr 3 Tl. *Physical Review B* **11,** 266 (1975).

17. Popescu, T. I. *et al. Zeeman split Kramers doublets in spin-supersolid candidate* $Na_2BaCo(PO_4)_2$ 2025. arXiv: `2503.00462 [cond-mat.str-el]`. `https://arxiv.org/abs/2503.00462`.

18. Newnham, R., Fang, J. & Santoro, R. Crystal structure and magnetic properties of CoTiO3. *Acta Crystallographica* **17,** 240–242 (1964).

19. Yuan, B. *Neutron Scattering Study of Magnetic Excitations in Quantum Magnets Bi2CuO4 and CoTiO3* PhD thesis (University of Toronto (Canada), 2021).

20. Cowley, R. *et al.* Neutron scattering investigation of the d- d excitations below the Mott gap of CoO. *Physical Review B—Condensed Matter and Materials Physics* **88,** 205117 (2013).

21. Pratt Jr, G. & Coelho, R. Optical absorption of CoO and MnO above and below the Néel temperature. *Physical Review* **116,** 281 (1959).

22. Haverkort, M., Tanaka, A., Tjeng, L. & Sawatzky, G. Nonresonant Inelastic X-Ray Scattering Involving Excitonic Excitations: The Examples of NiO and CoO. *Physical review letters* **99,** 257401 (2007).

23. Larson, B. C. *et al.* Nonresonant Inelastic X-Ray Scattering and Energy-Resolved Wannier Function Investigation of d-d Excitations in NiO and CoO. *Physical review letters* **99,** 026401 (2007).

24. Abragam, A. & Bleaney, B. *Electron paramagnetic resonance of transition ions* (OUP Oxford, 2012).

25. Sarte, P. *et al.* Ordered magnetism in the intrinsically decorated j eff= 1 2 α-CoV 3 O 8. *Physical Review B* **98,** 224410 (2018).

26. Stamokostas, G. L. & Fiete, G. A. Mixing of t 2 g-eg orbitals in 4 d and 5 d transition metal oxides. *Physical Review B* **97,** 085150 (2018).

27. Hutchings, M. T. in *Solid state physics* 227–273 (Elsevier, 1964).

28. Lane, H., Songvilay, M., Ewings, R. & Stock, C. Excitonic transverse and amplitude fluctuations in noncollinear and charge-ordered RbFe 2+ Fe 3+ F 6. *Physical Review B* **106,** 054431 (2022).

29. Haraldsen, J. T. & Fishman, R. S. Spin rotation technique for non-collinear magnetic systems: application to the generalized Villain model. *Journal of Physics: Condensed Matter* **21,** 216001 (2009).

30. Watanabe, T. *et al.* Elastic softness of low-symmetry frustrated A Ti 2 O 5 (A= Co, Fe). *Physical Review B* **111,** 024426 (2025).

31. Balbashov, A., Mukhin, A., Ivanov, V. Y., Iskhakova, L. & Voronchikhina, M. Electric and magnetic properties of titanium-cobalt-oxide single crystals produced by floating zone melting with light heating. *Low Temperature Physics* **43,** 965–970 (2017).

32. Sarte, P. *et al.* Disentangling orbital and spin exchange interactions for Co 2+ on a rocksalt lattice. *Physical Review B* **98,** 024415 (2018).

33. Harada, J. K., Balhorn, L., Hazi, J., Kemei, M. C. & Seshadri, R. Magnetodielectric coupling in the ilmenites M TiO 3 (M= Co, Ni). *Physical Review B* **93,** 104404 (2016).

34. Horsley, E., Rao, X., Yi, S. B. & Kim, Y.-J. Magnetic dilution of a honeycomb lattice XY magnet CoTiO3. *Journal of Physics: Condensed Matter* **34,** 135803 (2022).

35. Smart, J. S. & Van Vleck, J. H. Effective Field Theories of Magnetism. *Physics Today* **19,** 77–78. ISSN: 0031-9228 (Aug. 1966).

36. Stone, M., Zaliznyak, I., Reich, D. H. & Broholm, C. Frustration-induced two-dimensional quantum disordered phase in piperazinium hexachlorodicuprate. *Physical Review B* **64,** 144405 (2001).

37. Hase, M., Terasaki, I. & Uchinokura, K. Observation of the spin-Peierls transition in linear Cu 2+(spin-1/2) chains in an inorganic compound CuGeO 3. *Physical Review Letters* **70,** 3651 (1993).

38. Kageyama, H. *et al.* Exact dimer ground state and quantized magnetization plateaus in the two-dimensional spin system SrCu 2 (BO 3) 2. *Physical review letters* **82,** 3168 (1999).